

Magnetostatic spin-wave modes of an in-plane magnetized garnet-film disc

Eric R. J. Edwards*, Matthias Buchmeier, Vladislav E. Demidov, and Sergej O. Demokritov

*Institute for Applied Physics and Center for Nonlinear Science, University of Muenster,
Corrensstrasse 2-4, 48149 Muenster, Germany*

Macroscopic structures based on low-loss garnet films are an ideal model system for the space-resolved investigation of spin-wave dynamics. Here we investigate the dipolar eigenmodes of a garnet-film disc by means of scanning magneto-optical Faraday microscopy in the frequency domain. Due to the macroscopic dimensions of the studied samples, we have been able to image spatial profiles of the modes up to very high order. Our results show that the usual classification of eigenmodes based on their consideration as a product of standing waves in two orthogonal directions is not applicable in the case of in-plane magnetized disc samples. We find that the spatial distributions of the dynamic magnetization for the eigenmodes are strongly influenced by the intrinsic anisotropy of the dipolar spin-wave spectrum. Moreover, this leads to the appearance of caustic beams, whose directions are determined not by the sample shape, but by this anisotropy. These experimental results are corroborated by micromagnetic simulations, which accurately reproduce the salient features of the modes.

I. INTRODUCTION

The high-frequency magnetization dynamics of microscopic, laterally confined magnetic elements is today an active field of research (see, e.g., Refs. 1-7, as well as review of earlier work in Ref. 8). This activity is explained by the large potential of high-frequency magnetization dynamics for nano-scale transmission and processing of high-frequency signals⁹⁻¹³. Deep understanding of magnetization dynamics in confined geometries requires information about the spatial characteristics of dynamic magnetic modes, which is difficult to obtain for microscopic patterns because of the limited spatial resolution of the existing experimental techniques. In fact, the best spatial resolution in microwave-frequency magnetic measurements achieved so far using the

near-field magneto-optical microscopy¹⁴ is about 50 nm, which is comparable to lateral size of magnetic elements of interest.

A possible solution is to use larger magnetic structures as a model for space-resolved investigations of the dynamic magnetic modes¹⁵⁻¹⁶. This approach was widely used in the recent years to elaborate the principles of signal processing utilizing propagating waves of magnetization¹⁷ and led, for example, to the experimental demonstration of prototypes of such devices, as spin-wave logical gates¹⁸ and electronically controllable magnonic crystals¹⁹. The approach is based on the scaling of the spatial sizes of the studied structures to the millimeter spatial range and using low-loss insulating magnetic materials, such as yttrium iron garnet (YIG), to proportionally increase the characteristic decay length of spin waves. Although mono-crystalline YIG is not compatible with standard semiconductor technology, which hinders its applications in modern integrated electronics, due to its uniquely small dynamic magnetic damping, YIG films represent a perfect medium for basic research enabling observation of many novel dynamic magnetic phenomena²⁰⁻²².

The spin-wave dynamics is dominated by two coupling mechanisms, the long-range magnetostatic dipole interaction and the short-range exchange interaction. It is well known^{23,24} that a dipole problem is scalable, i.e. by scaling all the sizes of the element one does not change the spatial characteristics its dynamic magnetic eigenmodes. If both the dipolar and the exchange interactions are present, the scaling is not exactly valid. The ruling length scale for this situation is the exchange length,

$l_{ex} = \sqrt{A/\mu_0 M_s^2}$ which is typically of the order of 1 nm for ferromagnetic metals and several nanometers for YIG. The scaling provides reasonable results for modes with wavelengths much larger than l_{ex} which are dominated by the dipolar interaction and designated as magnetostatic modes⁸. Thus, the study of spin-wave eigenmodes in macroscopic YIG elements delivers valuable information about the magnetostatic eigenmodes in microscopic magnetic elements with comparable aspect ratios^{15,16}.

Herein we report on the experimental and numerical analysis of the spin-wave mode spectrum of a millimeter-sized, in-plane magnetized YIG disc. Using ferromagnetic resonance scanning magneto-optical Faraday microscopy, we have performed phase-sensitive imaging of the spatial structure of the modes up to very high order. The modes were found to exhibit wavevector quantization, although the two-

dimensional distribution of the dynamic magnetization cannot be decomposed into one-dimensional distributions.

The paper is organized as follows: In Sec. II we describe briefly the details of the sample, the experimental magneto-optical setup and the micromagnetic simulations. The results are presented and discussed in Sec. III. Finally, we summarize our results in Sec. IV.

II. EXPERIMENTAL DETAILS AND SAMPLE PREPARATION

The investigated samples were prepared from a 5.1 μm thick high-quality monocrystalline film of YIG grown on transparent gadolinium gallium garnet substrate. The ferromagnetic resonance (FMR) linewidth of the film (at 8 GHz) is $2\Delta B \cong 5 \cdot 10^{-2}$ mT, the saturation magnetization $\mu_0 M_s = 0.175$ T. The sample was chemically etched to produce a disc with a diameter of 1.3 mm. It was mounted on a computer controlled scanning stage and placed in the center of an electromagnet, capable of providing the static in-plane magnetic field $B=0\text{-}300$ mT, saturating the magnetization of the sample and tuning the eigenfrequencies of the spin-wave modes. In order to excite spin-waves, the sample was placed in the center of a circular loop copper microwave antenna, with an inner diameter of 2 mm. The excitation geometry is represented schematically in Fig. 1. Applying a microwave continuous-wave (CW) current to the loop, the antenna produces a microwave magnetic field b directed along the sample normal. Thus, the condition for linear excitation of the magnetization $\mathbf{b} \perp \mathbf{M}$ is fulfilled.

The magnetization dynamics was detected by stroboscopic imaging via magneto-optical Faraday-effect magnetometry synchronized with the microwave field. The approach used in the current study is similar to that reported in Refs. 25, 26. An oven controlled crystal oscillator generates a highly stabilized 10 MHz reference signal, which acts as a reference to generate both a sinusoidal microwave field, used to excite the spin-wave modes, as well as a 76 MHz signal used to synchronize the pulses of the Ti:sapphire laser. The time delay of the laser pulses with respect to the microwave signal was performed using a tunable phase shifter as shown in Fig. 1. In order to achieve synchronization of the microwave signal and the laser pulses, the microwave frequency must be a multiple of both the laser repetition rate 76 MHz and the 10 MHz reference frequency, i.e an integer multiple of 380 MHz. Throughout this paper we have

used a microwave frequency of 3.800 GHz. For the lock-in detection scheme, a series of microwave pulses with duration of 166 μ s and a repetition frequency of 3 kHz have been applied to the excitation coil. The average microwave power was varied from 10^{-5} mW to 1.6×10^3 mW.

The Ti-sapphire laser, a Mira 900 from Coherent Inc., has been operated at a wavelength of 820 nm, a pulse-duration of about 200 fs, pulse energy 13 pJ and an average power of less than 1 mW. The s-polarized incident laser beam was first widened by a beam expander and then focused to the sample surface with an achromatic lens. By scanning the laser spot over the sample edge and analyzing the intensity profile of the transmitted light, an optical resolution of 30 μ m, close to the theoretical resolution limit of 20 μ m of the optical system with a numerical aperture of $NA = 0.025$, has been determined. The Faraday rotation was measured using a differential detector system consisting of a $\lambda/2$ plate, a focusing lens, a polarizing beamsplitter, and two photodiodes. The probing spot was scanned in two lateral directions with a step size of 20 μ m across a 1.4 mm by 1.4 mm rectangular area covering the disc.

The angle of the Faraday rotation is proportional to the magnetization component parallel to the beam direction of propagation. For the used experimental geometry this means that the setup is sensitive to the out-of-plane component of the magnetization, M_{\perp} . In order to calibrate the detected Faraday rotation signal in terms of the out-of-plane magnetization angle, we have tilted the magnet by 15° out of the sample plane and recorded the remagnetization curve, measured by sweeping the applied magnetic field from -0.3 to 0.3 T and back. Using a single-domain model with literature values for the anisotropy constant and saturation magnetization to calculate the remagnetization curve, we are able to calibrate the measured Faraday signal. The experimental data shown below represent the dynamic out-of-plane magnetization normalized by M_s . In the rest of the paper we will refer the ratio $m_{\perp} = M_{\perp}/M_s$ as the out-of-plane precession angle.

III. MICROMAGNETIC MODELING

In lieu of analytic expressions determining the spin-wave spectrum of a disk with in-plane magnetization, we turn to micromagnetic modeling of the problem.

Micromagnetic simulations of the eigenmode spectrum have been carried out using the freely available OOMMF micromagnetics code²⁷. The program approximates the magnetization to be uniform inside the cells of a rectangular mesh. In order to minimize the artifacts due to this discretization and, on the other hand, achieve a reasonable computation time, the dimensions of the cells have to be optimized. As the experimental setup is mainly sensitive to the modes with quasi-uniform profile of the amplitude across the film thickness, we have chosen a perpendicular discretization stepsize equal to the film thickness. Together with an in-plane discretization of 10 μm , which is smaller than the optical resolution of the setup, this results in reasonable computation times of about 1 day using a standard PC.

We have assumed the literature values for the saturation magnetization, $\mu_0 M_s = 0.175$ T, the exchange constant, $A = 3.614 \times 10^{-12}$ J/m, the gyromagnetic ratio $\gamma = 2.21 \times 10^5$ m/(A·s), and the Gilbert damping parameter, $\alpha = 5 \times 10^{-5}$ (Refs. 28-29). The external field has been set to $B_{\text{ext}} = 70$ mT, found experimentally to match the main mode at the experimental excitation frequency of $\nu = 3.800$ GHz. The magnetization, relaxed previously to the ground state, has been excited with a weak, short, Hann-shaped DC-field pulse directed along the film-normal. In order to guarantee that only a linear response is produced, a low maximum strength of the exciting field of 10 μT has been applied. This results in a maximum out-of-plane precession angle of about 0.3×10^{-3} rad, a value which is one order of magnitude below the experimentally found nonlinearity threshold. The selected duration of the fieldpulse of 270 ps has a Fourier spectrum which is flat in the frequency range of the eigenmodes, between 3-4 GHz, therefore all excited modes correspond to a sinusoidal CW excitation of the same power and phase. In order to optimally resolve the dense spectrum of eigenmodes a long total simulation time of 800 ns yielding a frequency resolution of 0.125 MHz has been selected. The calculated maps of the magnetization have been stored at a sampling frequency of 20 GHz and converted with a discrete Fourier transformation into the frequency domain. In the experimental field range, the frequency is a linear function of the field, hence the spectra are subsequently converted into the field domain for direct comparison with experiment.

IV. RESULTS AND DISCUSSION

In an unconfined medium a uniform microwave field can only linearly excite

ferromagnetic resonance (the fundamental spin-wave mode with zero wavevector). All other spin-wave modes described by nonzero wavevectors and correspondingly varying frequencies cannot be excited under such conditions. In laterally confined films the situation is changed: (i) the spectrum of spin waves becomes quantized due to the finite size effect, which imposes selection rules on the in-plane wavevector; (ii) a spatially uniform microwave field of a given frequency can excite different spin-wave modes, albeit at different applied magnetic fields and with different effectiveness. Figure 2a illustrating the spin-wave spectrum in the studied YIG disc shows the measured out-of-plane precession angle as a function of the applied magnetic field. The upper curve represents the out-of-plane precession angle recorded at the sample center. One sees several peaks corresponding to different spin-wave modes. The most profound peak apparently corresponds to a fundamental spin-wave mode for this confined structure. Weaker peaks both at higher and lower applied fields indicate excitation of non-uniform modes. By recording this curve the phase of the microwave field has been adjusted to maximize the detected signal for the fundamental mode. Note that the phases of the spin-wave modes change alternatively with increasing or decreasing magnetic field. This is connected with excitation conditions of the corresponding modes by the spatially quasi-uniform microwave field.

Measurements at the center of the disc provide valuable information on the spin-wave modes. However, they also have essential drawbacks: (i) there is no information on the mode-profiles; (ii) the signal-to-noise ratio is rather poor. These disadvantages can be removed, if one maps the out-of-plane precession angle over the entire sample at a given applied field. First, the mode structure can be obtained in this way, as discussed below. Second, by integrating the squared out-of-plane precession angle over the sample one increases the signal-to-noise ratio as demonstrated by the lower curve in Fig. 2a, showing $\langle m_{\perp} \rangle = \sqrt{\iint m_{\perp}^2(y, z) dy dz}$. Up to 15 resonances are observed using this approach. Comparison of the resonance fields for different modes given by the upper and the lower curves in Fig. 2a indicates a very good agreement between the two techniques.

Figure 2b demonstrates the results of the modeling of the spin-wave dynamics in a YIG disk using the approach described above. One can see that modeling nicely reproduces the experimental data for the resonance fields for most of the modes, as

illustrated by the vertical dash lines in Figs. 2a and 2b corresponding to the theoretically determined resonance fields. Moreover, by analyzing the calculated mode profiles (see below) one can classify the modes by two integers (shown in brackets) indicating the number of antinodes on a line through the center of the sample perpendicular and parallel to the field, respectively. Apparently, the modeling shows only the spin-wave modes with odd antinode numbers. This fact is connected with the quasi-uniform spatial profile of the excitation field. In fact, the excitation efficiency of a mode with a given spatial profile of the out-of-plane magnetization $m_{\perp}(y,z)$ is proportional³⁰ the overlap integral of $m_{\perp}(y,z)$ with the excitation microwave magnetic field produced by the loop $h(y,z)$, $\iint h(y,z)m_{\perp}(y,z)dydz$. Since the field is quasi-uniform over the sample, only modes with an odd number of antinodes in either direction are efficiently excited. It is important to note that the effectiveness of the excitation decreases with increasing number of antinodes in the mode. Therefore, to analyze the general features of the modes with different symmetries, we have chosen modes with one antinode in one direction, since these modes should have higher excitation effectiveness. In general, modes with an even number of antinodes in either direction are not excluded by lateral confinement but require excitation by a spatially non-uniform microwave field¹⁵. One can also observe in Fig. 2a some additional modes, which apparently correspond to even numbers of the antinodes perpendicular to the magnetic field. The excitation of these modes is due to a non-uniform profile of the microwave field along this direction, caused by the inevitable disturbance of the axial symmetry by the leads of the excitation loop shown in in Fig. 1.

Analytical modeling of the spin-wave dynamics of an in-plane magnetized disc is extremely challenging task, since the axial symmetry of the sample is broken by the field. Nevertheless, to gain insight into general properties of the observed modes, it is constructive to compare them with the modes of an otherwise identical YIG square sample with side length equal the diameter of disc, d . In a square sample the two-dimensional profile of each mode can be factorized

$$m_{\perp}(y,z) = A \cos(k_y y) \cos(k_z z) = A \cos\left(\frac{n_y \pi}{d} y\right) \cos\left(\frac{n_z \pi}{d} z\right) \quad (1)$$

where n_y and n_z are the numbers of antinodes along the corresponding direction. The frequency of a spin wave with a wavevector defined by its in-plane components $\mathbf{k} =$

(k_y, k_z) can be calculated based on the theory for unconfined films³⁰, assuming a uniform spatial profile of the magnetization across the film thickness and small thickness of the film, t such that $kt \ll 1$,

$$\nu(k) = \gamma \sqrt{\left(B + \frac{k_y t}{2} \mu_0 M_s \frac{k_z^2}{k_y^2 + k_z^2} \right) \left(B + \mu_0 M_s \left(1 - \frac{k_y t}{2} \right) \right)} \quad (2)$$

Equation (2) describes the spin-wave modes in a particular confined sample, if one introduces the values of k_y and k_z , fulfilling the selection rules for this sample. Since the aspect ratio of the confined sample used in these studies $t/d = 4 \cdot 10^{-3}$ is small, one can neglect static demagnetizing effects here and consider B as the external magnetic field. To compare the experimental data with the dispersion given by Eq. (2), one should recall that the dipole interaction results in the pinning boundary conditions for dynamic magnetization at the lateral edges of a confined sample³¹. Therefore, the smallest allowed component of the wavevector in both directions is π/d , corresponding to the number of antinodes of 1. Taking into account this fact we have calculated the frequencies of the modes for $\mathbf{k} = (n_y \pi/d, n_z \pi/d)$ as shown in Fig. 3. Comparing Figs 2a and 3 one can conclude that this crude analytical model nicely describes the appearance of quantized modes at the fields both below and above the resonance field of the fundamental (1,1) mode. Moreover, Fig. 3 illustrates a possible degeneracy of different modes, for example of the (1,5) and (3,7) modes. The degeneracy results in a simultaneous excitation of these modes by the microwave field at a given external magnetic field. Space resolved measurements in this case provide a complex profile of the precession which essentially differs from a profile of a single mode (see the inset in Fig. 3).

Further comparison between the numerical modeling and the experiment can be made based on the mode profiles, as shown in Figs. 4 and 5. Figure 4 demonstrates the modes obtained at the magnetic field equal or lower than 72 mT, the resonance field of the fundamental (1,1) mode. We adopt the terminology of the so-called surface Damon-Eshbach (DE) modes as shorthand for describing these modes³², although the wavevectors characterizing these modes are not exactly perpendicular to the field. Nevertheless, in agreement with this classification alternative changes of the sign $m_{\perp}(y, z)$ are observed for these modes along the y-directions. The modes can apparently be identified as $(n_y, 1)$ -modes, n_y increasing with decreasing field. The situation with the

backward volume (BV) modes³² obtained for $B > 72$ mT is more complex, as illustrated in Fig. 5 for nominally $(1, n_z)$ -modes. On one hand, one observes that the number of antinodes increases with increasing field, as one expects from the negative group velocity of the BV-modes in an unconfined film. On the other hand, comparing the inset in Fig. 3 with the profile of mode (1,5) in Fig. 5 one can conclude, that the profiles presented in Fig. 5 correspond to a linear combination of two almost degenerate (1,5) and (3,7) modes. Similarly, mode (1,7) can be reproduced as a linear combination of (1,7) and (3,9) modes. At higher fields, the modes become increasingly complex, and are no longer simple linear combinations of two almost degenerate modes.

Concluding this section, let us notice that both experimentally measured and numerically simulated spatial profiles of the modes shown in Figs. 4 and 5 demonstrate X-like networks of crossing straight lines. The origin of the network, exemplarily shown in more detail in Fig. 6 for the experimentally measured profile of the (1,1)-mode, is scattering of spin waves by defects of the discs. Note here, that the network of rectangular cells used for simulation of a circular disk in micromagnetic calculations results in creation of defects on the contour of the disk. In fact, it is well known³³⁻³⁵ that the scattering of spin waves by a point defect results in formation of caustic beams due to a strong anisotropy of their dispersion. The process can be understood as follows: due to the anisotropy of the spin-wave dispersion the phase and the group velocity are not parallel to each other. While for a given frequency the direction of the phase velocity can vary in a wide interval of angles, the group velocity exhibits a certain preferential direction, determined by a critical angle θ_c . The scattering of spin waves by a point defect can be considered as re-radiation conserving the frequency of the wave, but not its wavevector. In this case, the re-radiated spin waves have the same frequency equal to the frequency of the mode, but different \mathbf{k} . Despite the large diversity in the direction of the phase velocity, which is parallel to \mathbf{k} , the radiated waves propagate along the preferential directions of the group velocity, which determines the flow of spin-wave energy. Thus, well defined beams along the direction defined by θ_c are built. Using the parameters of the experiment and applying the approach developed in Ref. 33, one can calculate the critical angle $\theta_c = 57^\circ$. The white lines in Fig. 6 corresponding to the calculated value of θ_c clearly demonstrate a very nice agreement between theory and experiment.

V. CONCLUSIONS

Using magneto-optical Faraday-microscopy we have imaged and investigated the magnetostatic spin-wave modes in a macroscopic YIG disc magnetized in plane. By sweeping the applied magnetic field at a constant excitation frequency we were able to detect up to 15 both Damon-Eshbach and backward-volume-like modes. Taking advantage of micromagnetic simulations based on the OOMMF software package we were able to reproduce the frequencies of the modes as well as their spatial profiles. Although the modes with small numbers of antinodes can be classified based on the more analytically tractable square-sample geometry, the profiles of the modes with large number of antinodes cannot be modeled as the product of two orthogonal standing waves, or a simple linear combination of almost degenerate modes. Caustic beams are observed on top of the mode profiles for different modes. Experimental results, including the caustic patterns, are convincingly reproduced in micromagnetic simulations.

ACKNOWLEDGEMENTS

We acknowledge support from Deutsche Forschungsgemeinschaft

References

1. F. Montoncello, L. Giovannini, F. Nizzoli, H. Tanigawa, T. Ono, G. Gubbiotti, M. Madami, S. Tacchi, and G. Carlotti, Phys. Rev. B **78**, 104421 (2008).
2. J. M. Shaw, T. J. Silva, M. L. Schneider, R. D. McMichael, Phys. Rev. B **79**, 184404 (2009).
3. V. E. Demidov, M. Buchmeier, K. Rott, P. Krzysteczko, J. Münchenberger, G. Reiss, and S. O. Demokritov, Phys. Rev. Lett. **104**, 217203 (2010).
4. V.V. Kruglyak, P. S. Keatley, A. Neudert, R. J. Hicken, J. R. Childress, and J. A. Katine, Phys. Rev. Lett. **104**, 027201 (2010).
5. H. Ulrichs, V. E. Demidov, S. O. Demokritov, and S. Urazhdin, Phys. Rev. B **84**, 094401 (2011).
6. K. Vogt, O. Sukhostavets, H. Schultheiss, B. Obry, P. Pirro, A. A. Serga, T. Sebastian, J. Gonzalez, K. Y. Guslienko, and B. Hillebrands, Phys. Rev. B **84**, 174401 (2011).
7. V. E. Demidov, S. Urazhdin, E. R. J. Edwards, M. D. Stiles, R. D. McMichael, and S. O. Demokritov, Phys. Rev. Lett. **107**, 107204 (2011).

8. S. O. Demokritov (Ed.): *Spin Wave Confinement* (World Scientific, Singapore, 2008).
9. V. E. Demidov, S. O. Demokritov, K. Rott, P. Krzysteczko, and G. Reiss, *Appl. Phys. Lett.* **92**, 232503 (2008).
10. S. Neusser and D. Grundler, *Adv. Mater.* **21**, 2927 (2009).
11. V. V. Kruglyak, S. O. Demokritov, and D. Grundler, *J. Phys. D: Appl. Phys.* **43**, 264001 (2010).
12. A. Khitun, M. Bao, and K. L. Wang, *J. Phys. D: Appl. Phys.* **43** 264005 (2010).
13. B. Lenk, H. Ulrichs, F. Garbs, and M. Münzenberg, *Physics Rep.* **507**, 107 (2011).
14. J. Jersch, V. E. Demidov, H. Fuchs, K. Rott, P. Krzysteczko, J. Münchenberger, G. Reiss, and S. O. Demokritov, *Appl. Phys. Lett.* **97**, 152502 (2010).
15. V. E. Demidov, U. Hansen, and S. O. Demokritov, *Phys. Rev. Lett.*, **98**, 157203 (2007).
16. M. Kostylev, V. E. Demidov, U. H. Hansen, and S.O. Demokritov, *Phys. Rev. B.* **76**, 224414 (2007).
17. A. A. Serga, A. V. Chumak, and B. Hillebrands, *J. Phys. D: Appl. Phys.* **43**, 264002 (2010).
18. T. Schneider, A. A. Serga, B. Leven, B. Hillebrands, R. L. Stamps and M. P. Kostylev, *Appl. Phys. Lett.* **92**, 022505 (2008).
19. A. V. Chumak, V. S. Tiberkevich, A. D. Karenowska, A. A. Serga, J. F. Gregg, A. N. Slavin, and B. Hillebrands, *Nature Commun.* **1**, 141 (2010).
20. S. O. Demokritov, V. E. Demidov, O. Dzyapko, G. A. Melkov, A. A. Serga, B. Hillebrands, and A. N. Slavin, *Nature* **443**, 430 (2006).
21. Y. Kajiwara, K. Harii, S. Takahashi, J. Ohe, K. Uchida, M. Mizuguchi, H. Umezawa, H. Kawai, K. Ando, K. Takanashi, S. Maekawa, and E. Saitoh, *Nature* **464**, 262–266 (2010).
22. Z. Wang, Y. Sun, M. Wu, V. Tiberkevich, and A. Slavin, *Phys. Rev. Lett.* **107**, 146602 (2011).
23. P. Bryant and H. Suhl, *Appl. Phys. Lett.* **54**, 2224 (1989).
24. L. D. Landau and E. M. Lifshitz, *Electrodynamics of Continuous Media* (Pergamon, Oxford, 1960).
25. S. Tamaru, J. A. Bain, R. J. M. van de Veerdonk, T. M. Crawford, M. Covington, and M. H. Kryder, *J. Appl. Phys.* **91**, 8034 (2002).

26. I. Neudecker, K. Perzlmaier, F. Hoffmann, G. Woltersdorf, M. Buess, D. Weiss, and C. H. Back, Phys. Rev. B, **73**, 134426 (2006).
27. M. J. Donahue and D. G. Porter, "OOMMF User's Guide, Version 1.0", National Institute of Standards and Technology, Interagency Report No. NISTIR 6376, (1999).
28. W. P. Wolf and G. P. Rodrigue, J. Appl. Phys. **29**, 105 (1958).
29. V. Cherepanov, I. Kolokolov, and V. L'vov, Phys. Rep. **229**, 81 (1993).
30. B. A. Kalinikos, IEE Proc. H **127**, 4 (1980).
31. K. Yu. Guslienko, S. O. Demokritov, B. Hillebrands, and A. N. Slavin, Phys. Rev. B, **66**, 132402 (2002).
32. R. W. Damon and J. R. Eshbach, J. Phys. Chem. Solids **19**, 308 (1961).
33. O. Büttner *et al.*, Phys. Rev. B **61**, 11576 (2000).
34. V.E. Demidov, S.O. Demokritov, D. Birt, B. O'Gorman, M. Tsoi, and X. Li, Phys. Rev. B **80**, 014429 (2009).
35. T. Schneider *et al.*, Phys. Rev. Lett. **104**, 197203 (2010).

FIGURE CAPTIONS

Fig1: Sketch of the sample arrangement and block-diagram of the experimental setup.

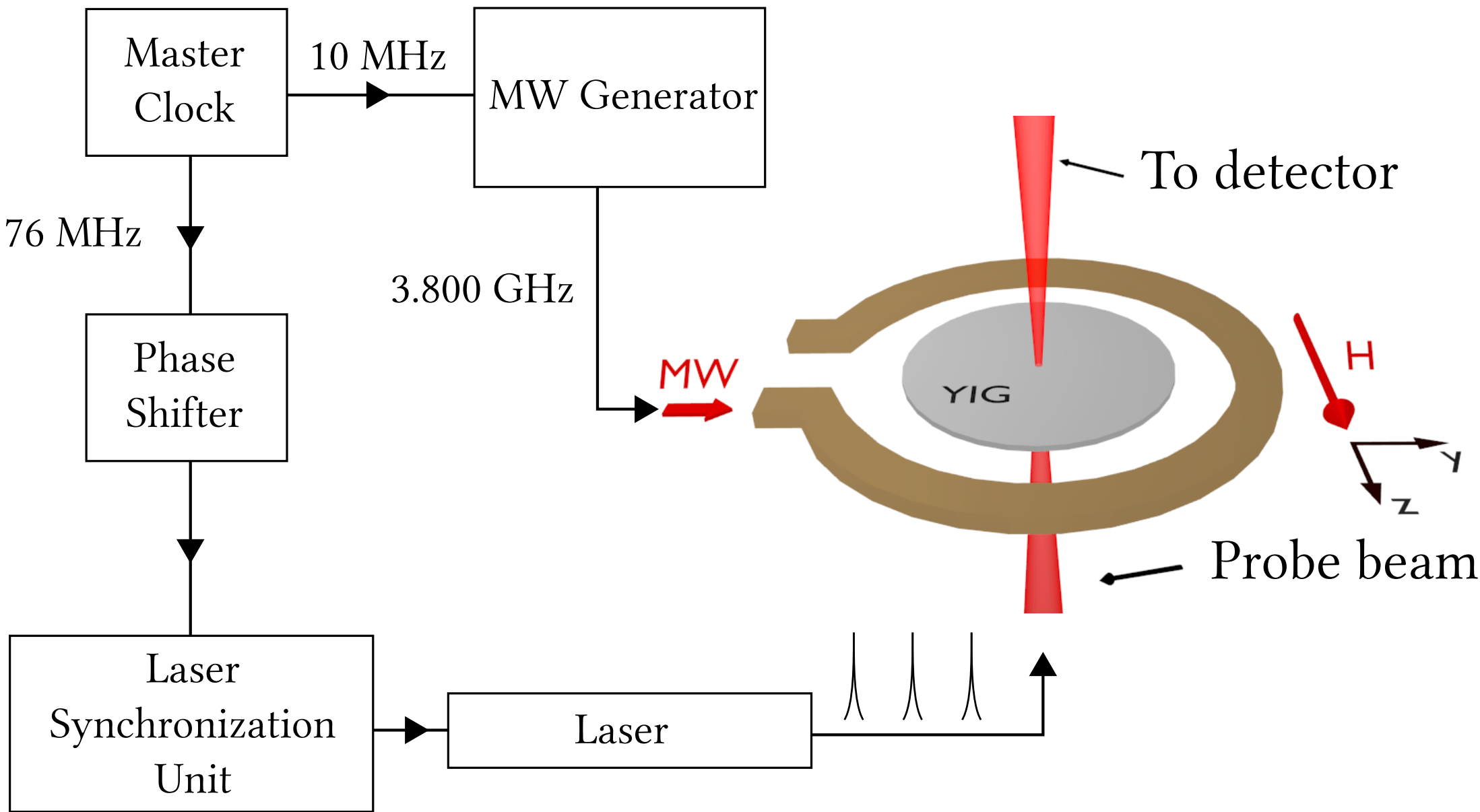
Fig2: (a) Field-swept spectrum recorded in experiment for microwave frequency 3.800 GHz. Filled curves represent data recorded with the laser spot fixed at the sample center. Points correspond to data obtained by integration over the sample. (b) the corresponding curves obtained using the OOMMF simulations

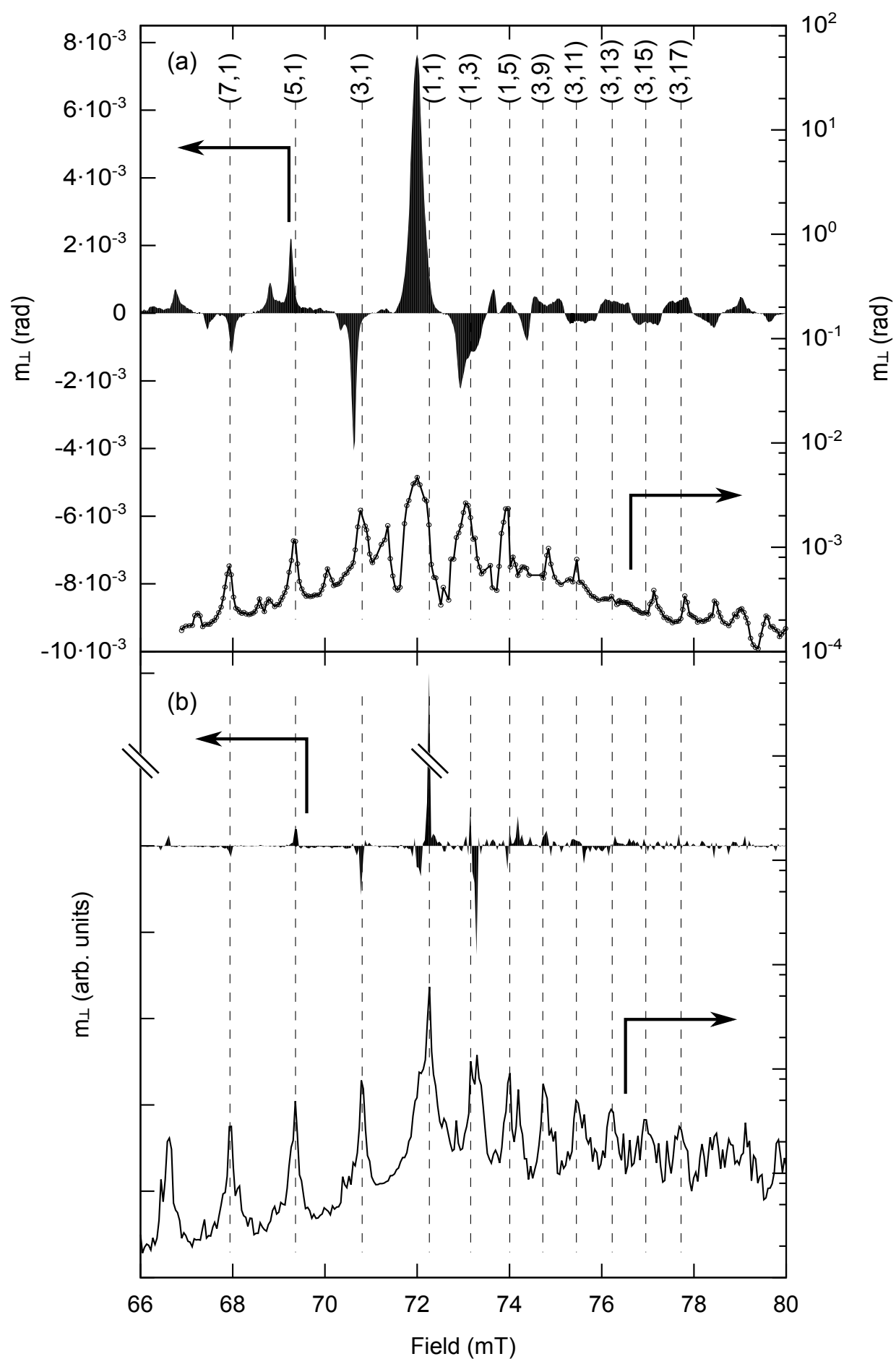
Fig3: Frequencies of the spin-wave modes in a square sample with different number of antinodes. Note partial degeneracy of different modes. Inset: calculated spatial profiles of the pattern formed by a linear combination of the (1,5)- and (3,7)-modes and (1,7) and (3,9) modes

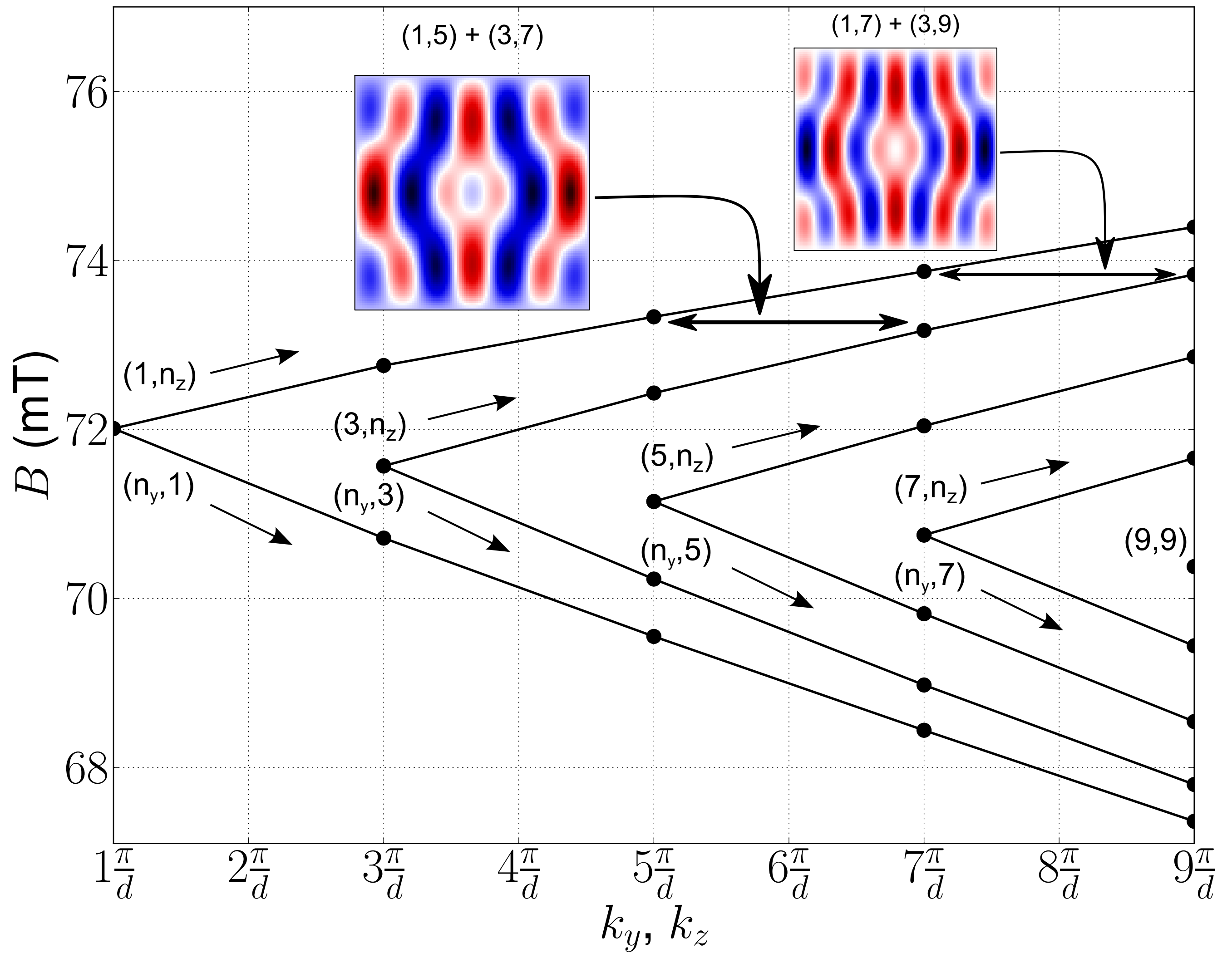
Fig4: Left, experimentally recorded spatial profiles for the fundamental (1,1)-mode as well as for the DE (3,1), (5,1), and (7,1) modes, respectively. Right, corresponding spatial profiles obtained via simulation with OOMMF. The resonance field for each mode at 3.800 GHz is indicated.

Fig5: Left, experimentally recorded spatial profiles for the BV (1,3), degenerate (1,5), and degenerate (1,7), modes, respectively. Right, corresponding spatial profiles obtained via simulation with OOMMF. The resonance field for each mode at 3.800 GHz is indicated.

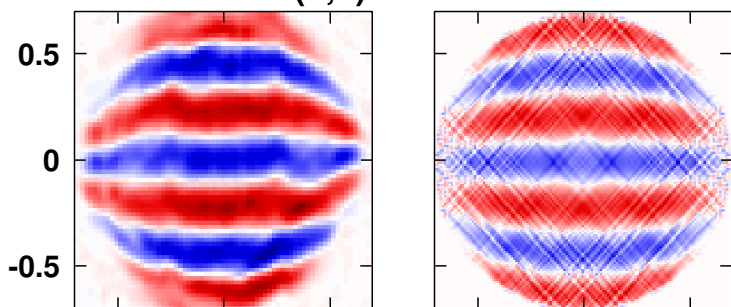
Fig6: Experimentally recorded spatial profiles of the fundamental (1,1) mode. Note the X-like network of straight lines. The white lines correspond to the calculated value of the critical angle $\theta_c = 57^\circ$.



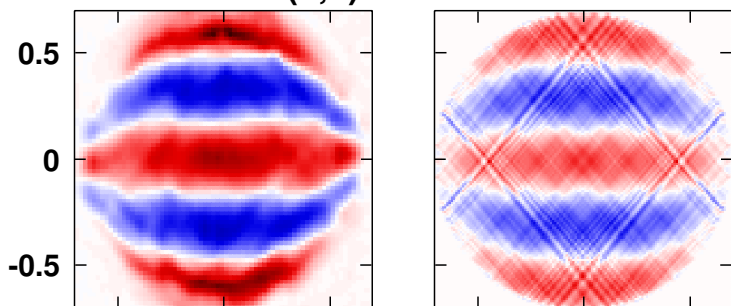




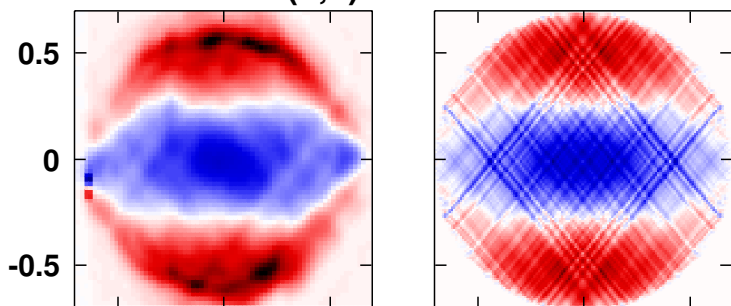
(7,1) 68.0 mT



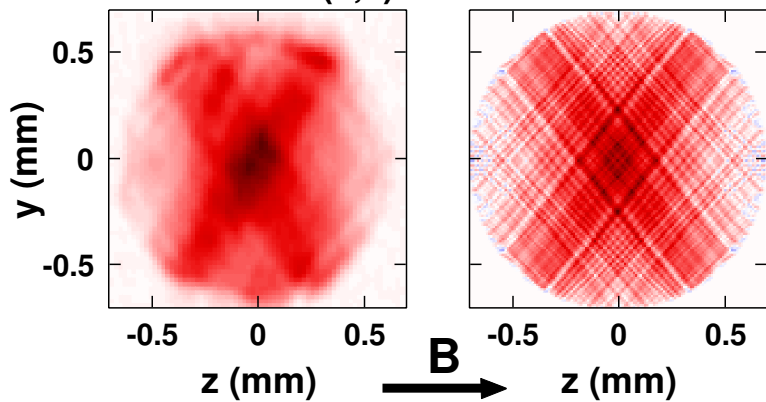
(5,1) 69.2 mT



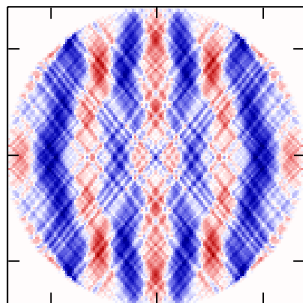
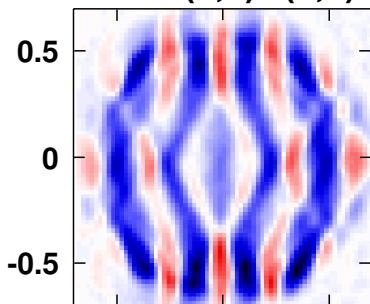
(3,1) 70.6 mT



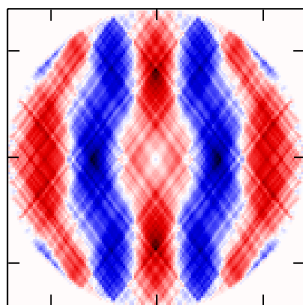
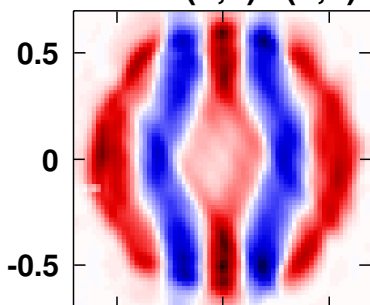
(1,1) 72.0 mT



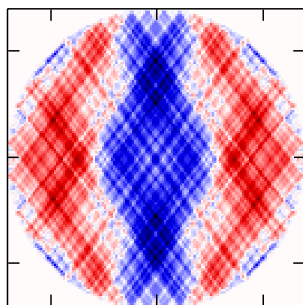
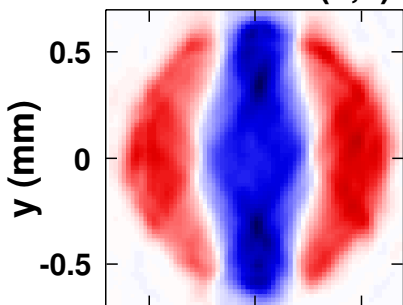
(1,7)&(3,9) 74.8 mT



(1,5)&(3,7) 73.9 mT



(1,3) 73.1 mT



z (mm)



z (mm)

